Metallocene/carbon hybrids prepared by a solution process for supercapacitor applications

Xianwen Mao, Fritz Simeon, Demetra S. Achilleos, Gregory C. Rutledge, and T. Alan Hatton**

Department of Chemical Engineering, Massachusetts Institute of Technology
77 Massachusetts Avenue, Cambridge
Massachusetts, 02139, USA
E-mail: tahatton@mit.edu, rutledge@mit.edu

Abstract

Efficient and scalable solution-based processes are not generally available to integrate well-studied pseudocapacitive materials (i.e., metal oxides and conducting polymers) with other components such as porous carbon, mainly because these classes of pseudocapacitive systems have poor solubilities in solvents and exhibit no specific interactions with the other component. Here we report, for the first time, the integration of a metallocene polymer, polyvinylferrocene (PVF), with carbon nanotubes (CNTs) via a simple solution process for supercapacitor applications. The solution processability of the PVF/CNT hybrid is due to the high solubilities of PVF in organic solvents and the unique ability of the metallocene/carbon system to form stable heterogeneous inks through the π-π stacking interactions between the two components. The nanostructure and electrochemical properties of the hybrid can be manipulated systematically by adjusting the composition of the heterogeneous ink. The hybrid with the optimized composition exhibits unusually high capacitance (1452 F/g) and energy density (128.9 Wh/kg) obtained in a standard two-electrode configuration, outperforming previously reported pseudocapacitive materials.

Broader Context

Supercapacitors with extremely high capacitance, enhanced energy and power densities, and excellent reliability offer great potential as complements to, and replacements for, batteries and conventional electrolytic capacitors for energy storage applications. Carbon nanomaterials, metal

oxides and conducting polymers have been investigated widely as supercapacitor electrode materials. Many emerging high-performance supercapacitor devices benefit from the integration of these different capacitive materials to exploit their synergies for enhanced capacitance and energy density. Meanwhile, solution processing is low-cost, high-throughput, and readily scalable. It is the preferred fabrication method for many devices such as solar cells, transistors, batteries and single-component supercapacitors, but is very difficult to use for the integration of either metal oxides or conducting polymers with other capacitive materials such as carbon nanotubes. Instead, the common integration methods rely for the most part on electrochemical deposition processes, which are time-consuming, low-throughput and difficult to scale up. In this study we have developed a metallocene/carbon hybrid system amenable to solution processing, with control of the nanostructure and electrocapacitive performance of the hybrid materials realized through manipulation of the ink composition. The optimized hybrid system, as determined by its composition, consists of a highly porous nanoscale architecture in which a three-dimensional conductive carbon nanotube network with interconnected nanopores is coated conformally by the redox-active metallocene polymer. This unique morphology simultaneously facilitates electron transport, reduces ion diffusion length, and increases metallocene utilization efficiency. Thus this hybrid exhibits significantly improved electrochemical performance compared to the performance of the individual components alone. A standard two-electrode supercapacitor cell constructed with this hybrid system shows extremely high specific capacitance and energy density. The unusually high capacitive energy storage capabilities of the metallocene/carbon hybrid, in combination with its unique solution processability, make it one of the best material systems for the development of low-cost high-performance supercapacitor devices.

Introduction

Supercapacitors have attracted widespread attention as promising energy storage devices due to their high capacitance, long cycle life, fast response time, and exceptional reversibility and reliability.[1, 2] These advantages allow supercapacitors to meet the challenge of delivering high currents in heavy-duty systems such as hybrid electric vehicles and large industrial equipment.[3] The large specific capacitance of supercapacitors results from two charge-storage mechanisms that occur at the electrode/electrolyte interface: double-layer capacitance, which is a non-Faradic process, and redox-based pseudocapacitance, which is a Faradic process. These two mechanisms can work separately or together. Carbon-based materials are well-known examples of double-layer capacitive materials,[1, 2, 4] while conducting polymers and metal oxides have been studied extensively as pseudo-capacitive materials.[1, 2, 5] Recently, heterogeneous nanostructured materials have emerged as promising systems for electrochemical energy storage, due to the combined benefits of reduced inherent structure size of the bulk materials (e.g., enhanced specific surface area and reduced ion diffusion length) and synergy of the properties of the individual components (e.g., improved electron transport efficiency and mechanical stability).[6, 7] Hybrid nanostructures have been created by controlled assembly of different capacitive materials, such as conducting polymer/carbon,[8-14] conducting polymer/metal oxide,[15] metal oxide/carbon,[16-18] metal oxide/metal oxide,[19] and metal oxide/metal,[20-22] and have been reported to exhibit extremely high capacitances as well as improved energy and power densities. When constructing these heterogeneous systems, the ability to manipulate their composition and nanoscale architecture, and to assemble the individual components in a way that does not impair their respective advantageous features (e.g., preservation of intrinsically high conductivity of the conducting component), plays a key role in the optimization of their electrocapacitive performance.[8-22]

Low-cost, high-throughput, and readily scalable solution processes have been exploited to deposit various nanomaterials on appropriate substrates for large-scale applications, including

solar cells,[23, 24] thin-film transistors,[25-27] lithium-ion batteries,[28, 29] and single-component supercapacitor devices.[29, 30] However, it is very difficult to employ solution processes to construct heterogeneous nanomaterials based on well-studied pseudo-capacitive materials (i.e., metal oxides and conducting polymers), especially those with controlled morphology and electrocapacitive properties.[5-7] This is due to the poor solubilities of metal oxides and conducting polymers in most solvents, and lack of strong interactions between these pseudo-capacitive materials and other components, such as carbon nanotubes (CNTs) and graphene.[31, 32] Thus, in general, different capacitive materials cannot form stable complexes in solvents, and it is difficult to generate well-dispersed, high-quality heterogeneous "inks" for solution processing. The common techniques for integrating conducting polymers[8-13, 15] or metal oxides[15, 17-22] with other components rely heavily on electrochemical deposition or co-deposition of their precursors (i.e., solublized monomers or metal ions, respectively). These methods use electrochemical synthesis conditions to manipulate the nanostructures and thus electrocapacitive properties of the resulting heterogeneous materials. As such, these strategies require the use of complicated electrochemical set-ups and sometimes multi-step post-processing such as template removal,[15] and thus can be time-consuming, of low-throughput, and difficult to scale up.

Here we show that a metallocene-containing polymer, polyvinylferrocene (PVF), can be integrated with pristine carbon nanotubes via a simple, rapid, scalable, solution-based process. The nanoscale architecture and electrochemical properties of the resulting PVF/CNT hybrid can be manipulated easily and systematically by adjusting the composition of the precursor ink. The hybrid with an optimized composition exhibits a highly porous nanostructure, It consists of a three-dimensional conductive CNT framework with interconnected nanopores, coated conformally by the energy-dense redox-active metallocene polymer. This unique structure facilitates electronic/ionic transport and enhances metallocene utilization efficiency. Therefore

this hybrid shows significantly improved energy storage properties compared to those of the individual components alone. A standard two-electrode supercapacitor cell constructed with this hybrid exhibits a specific capacitance of 1452 F/g and an energy density of 128.9 Wh/kg; the two values are significantly higher than those of previously-reported pseudocapacitive materials (**Supporting Information Table S2**).

The solution processability of the PVF/CNT system is due to its unique ability to form stable, well-dispersed multi-component inks through the noncovalent, π-π stacking interactions between the cyclopentadiene (Cp) rings of the ferrocene moieties in PVF and the sp^2-conjugated surfaces of CNTs.[33] Such π-π stacking interactions generally exist between various conductive nanocarbons with sp^2-conjugated surfaces (e.g., graphene, fullerenes, and carbon nanotubes) and molecular systems containing metallocenes with Cp rings (e.g., MCp_2, M = Fe, Co, Mn, V, Cr, etc.) that can undergo fast and reversible redox reactions. Therefore, in contrast to conducting polymer- and metal oxide-based pseudocapacitive composite materials, the metallocene/carbon system represents a new class of heterogeneous energy-storage materials that is amenable to solution-based construction.

The metallocene/carbon system also enjoys a number of other advantages for supercapacitor fabrication. Firstly, in contrast to chemical modification, the noncovalent assembly method maintains the sp^2-conjugated surfaces of nanocarbons, which play a key role in facilitating electron transport in the hybrid systems. Secondly, the fabrication of the hybrid system employs a process that is binder-free, surfactant-free, and substrate-independent. Therefore, this method avoids issues associated with surfactant removal (such as reduced conductivity and mechanical integrity of the deposited film), and can be extended to stretchable substrates, making it useful for the development of flexible electronics.[29]

Results and Discussion

The PVF/CNT hybrids were fabricated through deposition of the PVF/CNT ink (obtained via gentle sonication) on solid substrates followed by solvent evaporation. **Figure 1a** illustrates this fabrication process schematically. For experimental details, see **Supporting Information Section S1.2**. The nanostructure of the hybrid can be manipulated by varying systematically the PVF/CNT mass ratio in the precursor ink before deposition. As this ratio decreases, the dominant species in the ink changes from free polymers, to PVF/CNT complexes, to non-functionalized CNTs. This leads to morphological transitions in the deposited hybrids from a thick polymer film with buried nanotubes, to a porous CNT network with conformal polymer coating, to a CNT mat with little polymer exposed. Hereafter a hybrid containing *X*% PVF and *Y*% CNT (weight percent, $X + Y = 100$) is denoted as PVF_X/CNT_Y. **Figure 1b** shows that in the absence of PVF, the suspended CNTs precipitate out within a few days, whereas PVF/CNT inks of various compositions exhibit good stability over at least a month, which is sufficient for the rapid fabrication process. A typical transmission electron microscopy (TEM) image (**Figure 1c**) of a PVF/CNT ink (0.80 mg mL^{-1} PVF and 0.20 mg mL^{-1} CNT) shows that most CNTs are completely de-bundled individual tubes. PVF/CNT inks with other compositions exhibit similarly good dispersion of nanotubes when inspected by TEM.

The morphologies of the PVF/CNT hybrids with various compositions were investigated by high-resolution scanning electron microscopy (HR-SEM) and atomic force microscopy (AFM). As evident from the HR-SEM images in **Figure 2a,** the diameters of the tubular entities decrease when the polymer weight percent is reduced from 97% to 80% to 33%. In PVF_{97}/CNT_3, the CNTs are buried deeply in the polymer films. In contrast, PVF_{80}/CNT_{20} exhibits interconnected nanopores with conformal polymer layers coating the three-dimensional CNT framework. The morphology of PVF_{33}/CNT_{67} is very similar to that of depositions involving only unmodified CNTs (**Supporting Information Figure S7**), suggesting that the extent of polymer coating on

CNTs in PVF_{33}/CNT_{67} is very low and that there may be unmodified nanotubes exposed on the surface. The AFM (amplitude) images of the hybrids are shown in **Figure 2b**. Here, we observe a general trend of decreasing tube diameters with lower PVF content. However, the diameter difference between PVF_{97}/CNT_3 and PVF_{80}/CNT_{20}, as probed by AFM, is not as obvious as the difference revealed by HR-SEM. Notably, the average tube diameters for PVF_{80}/CNT_{20} shown in the AFM image appear slightly larger than the diameters shown in the HR-SEM image. This may be due to artifactual broadening oft he AFM scan since the tip cannot penetrate the pores to measure the surface of the CNT framework accurately. For PVF_{97}/CNT_3 and PVF_{80}/CNT_{20}, the average tube diameters are consistent between the HR-SEM and AFM analyses, possibly because these two hybrids exhibit fewer surface features, and thus the tip broadening effects are not pronouced. Moreover, in the AFM image of PVF_{97}/CNT_3, we observed some areas with almost no AFM contrast (as indicated by the black rectangles), which resemble the image of a pure PVF film (**Supporting Information Figure S8**). This indicates that regions composed of pure polymer exist in PVF_{97}/CNT_3; with the CNT content as low as only 3%, PVF films are not effectively penetrated by the nanotubes.

We also examined the surface chemical compositions of the PVF/CNT hybrids using X-ray photoelectron spectroscopy (XPS). **Figure 3** shows the Fe/C ratios obtained on the surfaces of the hybrids as a function of CNT weight percent, calculated from their XPS spectra. For XPS quantification details, see **Supporting Information Section S1.5**. Pure PVF has a Fe/C ratio of 0.02, while the pristine CNTs have no iron signal (Fe/C ratio is equal to zero). The PVF/CNT hybrids with the CNT content ranging from 3% to 50% have the same Fe/C ratios as the pure polymer. This indicates that the surfaces of these hybrids are covered completely by PVF. It is of particular impartance that PVF_{80}/CNT_{20} has the same surface chemical composition as the neat polymer, despite its highly porous nanostructures as revealed HR-SEM. This indicates that the

CNT scaffold is *conformally* coated by PVF, and almost no unmodified nanotubes are exposed on the surface. In contrast, when the CNT weight percents are as high as 67% and 90%, the Fe/C ratios decrease markedly to 0.012 and 0.005, respectively. This suggests that the surfaces of these two hybrid systems are only partially covered by the redox polymer and may consist of both PVF-coated nanotubes and unfunctionalized CNTs.

Next we tested the electrochemical properties of the PVF/CNT hybrids of various compositions in a three-electrode system with 0.5 M $NaClO_4$ as the electrolyte. The hybrids exhibit highly reproducible composition-dependent electrocapacitive properties; the results are summarized in **Figure 4**. **Figure 4a** shows the specific capacitances of the PVF/CNT hybrids as a function of CNT weight percent. The specific capacitance first increases with CNT content between 0 wt% and 20 wt%, and then decreases with further increases in the CNT content from 20 wt% to 100 wt%. PVF alone shows a very low capacitance of 57 F g^{-1}, possibly due to its low conductivity and small surface area, which suggests inefficient utilization of the redox-active ferrocene moieties. The pristine CNTs also have a very low capacitance of 16 F g^{-1}. Remarkably, the PVF/CNT hybrids exhibit significantly greater capacitances than either component alone, with a peak value of 335 F g^{-1} at a CNT composition of 20 wt%. This optimal capacitance value may be attributed to the unique morphology of PVF_{80}/CNT_{20} (**Figure 2, $\mathbf{PVF_{80}/CNT_{20}}$**), in which the three-dimensional porous CNT network is coated conformally with PVF. The highly conductive CNT framework facilitates electron transport to favor the redox transformation of ferrocene, while the porous structure allows easy ion diffusion into the polymer layer. Moreover, the conformality of the polymer coating exposes a high density of redox sites to the electrolyte solution. When the CNT weight percent is further increased to 67%, the polymer coating is less obvious (**Figure 2, $\mathbf{PVF_{33}/CNT_{67}}$**), indicating a low density of redox-active species exposed on the surface. This results in a reduction of capacitance to 109 F g^{-1}. On the other hand, when the

CNT content is as low as 3%, the nanotubes are buried in thick polymer films with low porosity (**Figure 2, PVF_{97}/CNT_3**), which leads to a reduction of capacitance to 179 F g^{-1}.

The dramatically improved energy storage capacity of the PVF/CNT hybrids can be directly appreciated by comparing their cyclic voltammetric (CV) responses with those of pure PVF and pristine CNTs, respectively. The CV curves are shown in **Figure 4b**. CNTs alone exhibit a rectangular voltammogram, characteristic of double-layer capacitive materials. The cyclic voltammogram of PVF shows two redox peaks, indicative of pseudocapacitive behavior. Compared to pure PVF and CNTs, the three PVF/CNT hybrids exhibit significantly enhanced current response; among them, PVF_{80}/CNT_{20} exhibits the highest current density. The correlations of the specific capacitance with the scan rate is shown in **Figure 4c**. For a given scan rate, the PVF/CNT hybrids outperform both the pure PVF and unmodified CNTs, with PVF_{80}/CNT_{20} showing the highest capacitance values over the entire scan range.

The galvanostatic measurements are shown in **Figure 4d**. CNTs alone show a linear decrease with time over the entire potential range from 0.8 to 0.0 V, suggestive of typical double-layer capacitive behavior with no Faradaic contribution, whereas PVF-containing samples display sloped plateaus between 0.5 and 0.1 V, corresponding to the pseudocapacitive contribution from the redox reactions of ferrocene. PVF_{80}/CNT_{20} shows the longest discharge time when the potential varies from 0.8 to 0.0 V, indicating that it has the highest capacitance among all samples. **Figure 4e** shows that, over a wide range of current densities from 2.5 to 40 A g^{-1}, the PVF/CNT hybrids exhibit much higher capacitances than neat PVF and CNTs, respectively. For the three hybrid systems, the capacitive performance is improved, in the order PVF_{33}/CNT_{67} < PVF_{97}/CNT_3 < PVF_{80}/CNT_{20}; this is consistent with the cyclic voltammetry tests (**Figure 4c**). Moreover, PVF_{80}/CNT_{20} retains 90% of its capacitance (275 F g^{-1} from 306 F g^{-1}) as the current density increases from 2.5 to 40 A g^{-1}, while PVF alone retains only 31% of its capacitance (from

35 F g^{-1} to only 11 F g^{-1}) over the same current range. PVF_{97}/CNT_3 and PVF_{33}/CNT_{67} retain 83% and 84% of their capacitances, respectively. The improved rate performance of the hybrids, compared to that of PVF, may be attributed to the incorporation of the conductive CNT component, which facilitates electron transport through the polymer film. In addition, we found that the effects of the substrate and of the loading mass of the active materials on the electrochemical performance of the PVF/CNT hybrids are negligible (**Supporting Information Section S2**).

Based on the initial screening of the hybrids with varying compositions, we found that PVF_{80}/CNT_{20} exhibits optimal capacitive performance due to its porous CNT network with conformal polymer coating. To elucidate the positive effects of its unique nanostructure on the performance of PVF_{80}/CNT_{20}, further electrochemical characterization was carried out; the results are shown in **Figure 5**. Firstly, we compared the utilization efficiency of redox-active sites (i.e., ferrocene moieties) in PVF_{80}/CNT_{20} to that in PVF. This is important since a higher efficiency, i.e., more electrochemically active ferrocene molecules, can result in enhanced pseudocapacitance. Chronocoulometry was used to quantify the ferrocene utilization efficiency, defined as the ratio of the observed charge due to ferrocene oxidization to the theoretical value when all ferrocenes are oxidized (for details, see **Supporting Information Section S1.6**). **Figure 5a** shows the ferrocene utilization efficiency versus time of oxidation (0.5 V versus Ag/AgCl) for PVF_{80}/CNT_{20} and PVF. Compared to the plateau value obtained for PVF alone (8%), the ferrocene utilization efficiency for PVF_{80}/CNT_{20} is significantly higher, at 63%. This is attributed to the highly porous structure and enhanced surface area of PVF_{80}/CNT_{20}, which creates a thin polymer layer around its CNT scaffold; the specific surface area of PVF_{80}/CNT_{20} is determined to be 112 m^2 g^{-1} by the Brunauer-Emmmett-Teller method from the nitrogen adsorption isotherm, which is much higher than the value obtained for PVF alone (8 m^2 g^{-1}). Therefore, more

ferrocenes contact both the electrolyte solution and the conductive framework, and thus more are electrochemically active.[34] Secondly, we measured the charging resistances in electrolyte solution for both PVF_{80}/CNT_{20} and PVF from electrochemical impedance spectroscopy (EIS). For details, see **Supporting Information Section S1.7**. **Figure 5b** shows that the charging resistance of PVF_{80}/CNT_{20} is reduced significantly compared to that of PVF alone, in particular in the low frequency regime (10 – 100 Hz), indicating efficient propagation of the EIS *ac*-signal in PVF_{80}/CNT_{20}. This can be attributed to the shortened electrolyte pathways associated with the interconnected, electrolyte-filled nanopores that are characteristic of the unique structure of PVF_{80}/CNT_{20}. The reduced charging resistance may also explain the improved rate capability of PVF_{80}/CNT_{20} when compared to that of PVF, as evidenced in **Figure 4e**. Furthermore, the cycling stability of PVF_{80}/CNT_{20} was investigated by constant current charge/discharge experiments at a current density of 5 A g^{-1}. **Figure 5c** shows that its specific capacitance decreases only 9% after1500 cycles, demonstrating very good electrochemical stability. The cyclic voltammetric responses of PVF_{80}/CNT_{20} after the 1^{st}, 200^{th}, 600^{th}, and 1500^{th} cycle are shown in **Figure 5c inset**. It can be seen that the integral area of the cyclic voltammogram after multiple charge/discharge cycles decreases only marginally with increasing number of cycles. In contrast, the capacitance of PVF decays by 62% after the cycling experiments under the same conditions. The improved cycling stability of PVF_{80}/CNT_{20} may be ascribed to the mechanical integrity of the interconnected nanotubes, which support the polymer layers and prevent large morphological changes during the charge/discharge process.

We hypothesize that the facile preparation of the metallocene/carbon hybrids based on their noncovalent interactions preserves the sp^2-conjugated structure of the conductive carbon component. This guarantees fast electron transport in the hybrids and efficient redox transformation of the pseudocapacitive metallocene species, which are crucial for enhanced

power and energy densities, respectively. To prove this hypothesis, we examined the microstructure of the nanotube component in PVF_{80}/CNT_{20}; the results are shown in **Figure 6**. Disruption of the sp^2 carbon surface by covalent modification can lead to an increase in the I_D/I_G ratio detected by Raman spectroscopy due to the generation of sp^3 defect sites.[35] Generation of additional defects during preparation of the hybrids was not observed in our case, however; as shown in the Raman spectra (**Figure 6a),** the I_D/I_G ratio of PVF_{80}/CNT_{20} remains the same as that of the pristine carbon nanotubes. This result indicates that our fabrication process does not destroy the sp^2 conjugated structures of the CNT component. For calculation of the I_D/I_G ratio, see **Supporting Information Section S1.8**. In addition, the X-ray diffraction (XRD) pattern of PVF_{80}/CNT_{20}, shown in **Figure 6b**, displays a characteristic peak at $2\theta = 26°$, corresponding to diffraction from the graphite-like lattices of these multiwalled CNTs.[36, 37] This suggests that the lattice structure of the nanotube component is not destroyed in the preparation of PVF_{80}/CNT_{20}. **Figure 6c** shows the normalized ultraviolet photoelectron spectra (UPS) of PVF_{80}/CNT_{20} and untreated CNTs. The valence band structures of PVF_{80}/CNT_{20} resemble those of untreated CNTs. Both exhibit a broad peak from 0 to 12 eV and a sharp peak from 12 to 17 eV, corresponding to mixed $p\pi$-$p\sigma$ bands and *s*-like σ bands, respectively.[38, 39] This indicates that the electronic structures of the nanotube component are mostly preserved in PVF_{80}/CNT_{20}, in sharp contrast to other cases in which covalent modifications of CNTs are employed.[40, 41] A close examination of the UPS spectra reveals that the density of π electronic states (0 – 5 eV)[38, 39] in PVF_{80}/CNT_{20} is greater than that in pristine CNTs, possibly because the π electron density of the sp^2 hybridized nanotube walls is enhanced by stable interactions with the ferrocene moieties; ferrocenes have been shown to exhibit a strong π electron-donating ability.[42] Moreover, the work function of PVF_{80}/CNT_{20} (4.54 ± 0.06 eV, s.d.), calculated from the UPS spectra (see **Supporting Information Section S1.9**), is higher than that of untreated CNTs (3.95 ± 0.02 eV, s.d.). This

increase in the work function may be attributed to the creation of a surface dipole by adsorption of the ferrocene moieties in PVF_{80}/CNT_{20}. Because the nanotube surfaces are in close contact with the negatively-charged cyclopentadiene rings, an induced dipole field is generated; this dipole opposes electron emission from the CNT surfaces, thereby increasing the work function.[43]

Finally, we evaluated the supercapacitor cell performance of PVF_{80}/CNT_{20} in a two-electrode configuration with the standard 1 M H_2SO_4 aqueous electrolyte; the results are shown in **Figure 7a**. Acidic electrolytes are commonly employed for supercapacitors based on pseudocapacitive materials (**Supporting Information Table S2**), since they usually provide higher capacitances than do neutral electrolytes.[44] The thickness of the active materials (i.e., PVF_{80}/CNT_{20}) in our supercapacitor cell is ~22 μm (measured by SEM cross-sectional analysis), consistent with the recommended value of 15 μm for commercial supercapacitor devices.[45] **Figure 7b inset** shows the cyclic voltammetric responses of PVF_{80}/CNT_{20} and PVF. The CV curves of PVF_{80}/CNT_{20} exhibited a non-rectangular shape, indicative of pseudocapacitive behavior**.** When tested at the same scan rate (20 mV/s), PVF_{80}/CNT_{20} supported a much higher current density than did PVF. **Figure 7b** shows the specific capacitance of PVF_{80}/CNT_{20} as a function of scan rate, derived from the cyclic voltammetric measurements. PVF_{80}/CNT_{20} exhibits an extremely high capacitance of 1241 F/g at a scan rate of 20 mV/s, and a modest value of 190 F/g at a very high scan rate of 200 mV/s. The constant-current discharge profiles of PVF_{80}/CNT_{20} at different current densities are shown in **Figure 7c inset**. Galvanostatic measurements have been considered the most accurate method for determining the capacitance for supercapacitor materials.[45] **Figure 7c** shows the specific capacitance of PVF_{80}/CNT_{20} versus the current density, calculated from the galvanostatic discharge profiles. A high capacitance value of 1450 F/g was obtained at a high current density of 20 A/g, and a capacitance value of 195 F/g was obtained at an even higher current density of 80 A/g. The optimal capacitance value for PVF_{80}/CNT_{20} (1450

F/g) is comparable to the highest values reported to date for pseudocapacitive materials obtained in a two-electrode configuration (e.g., 911 F/g for brush-like Co_3O_4,[46] and 1145 F/g for MnO_2/nanoporous gold[20]). It should be noted that many previously reported high capacitance values (~1000-3000 F/g) based on conducting polymers[10-12] and metal oxides[16, 19, 21, 22] are obtained in a three-electrode configuration, which can be subject to errors in the measurement of capacitance, in particular for pseudocapacitive systems.[45] A more complete list of the electrocapacitve performances of different pseudocapacitive materials is shown in **Supporting Information Table S**2. Moreover, it can be seen from Table S2 that most high capacitance values are obtained at low operation rates (less than 1 A/g). Therefore, PVF_{80}/CNT_{20} exhibits the best combination of high capacitance and high operation rate (1450 F/g at 20 A/g) among currently available pseudocapacitive materials. We attribute this to its unique nanoscale architecture, in which a porous conductive CNT network is coated conformally with a thin, redox-active polymer layer. This architesture allows easy and efficient transport of both electrons and ions, which in turn affords fast redox reactions at high rates. **Figure 7d** shows the Ragone plot for PVF_{80}/CNT_{20} and the power and energy density ranges for common classes of energy storage devices.[47] It can be seen that the energy densities of the PVF_{80}/CNT_{20}-based device are comparable to those of batteries, while its power densities are maintained at values as high as those observed with conventional electrolytic capacitors.[47] The maximum energy density (128.9 Wh/kg), which is achieved at a reasonably high power density (16.6 kW/kg), represents the highest reported value among pseudocapacitive materials in aqueous electrolytes with a typical electrochemical window ~1V (**Supporting Information Table S2**).

Conclusion

We have developed a metallocene/carbon hybrid system that can be constructed by an economical, rapid, scalable, solution-based process for supercapacitor applications. The

nanostructure and electrochemical properties of this hybrid can be manipulated systematically by adjusting the composition of the heterogeneous ink. The ease of assembly oft he metallocene/carbon hybrid contrasts sharply with that of metal oxide- and conducting polymer-based heterogeneous systems, in which their controlled aseembly relies heavily on electrochemical deposition processes that are low-throughput and hard to scale up. Moreoever, the PVF/CNT hybrid with the optimized composition exhibits a highly porous nanoscale architecture in which a three-dimensional conductive carbon nanotube network with interconnected nanopores is coated conformally by the redox-active metallocene polymer. This unique morphology simultaneously facilitates electron transport, reduces ion diffusion length, and increases metallocene utilization efficiency. Thus this hybrid exhibits significantly improved electrochemical performance compared to those of the neat individual components. A standard two-electrode supercapacitor cell constructed with this hybrid system shows extremely high specific capacitance and energy density. The exceptional electrocapacitive energy storage capabilities of the metallocene/carbon hybrid, accompanied by its unique solution processability, make it an excellent material system for the development of low-cost high-performance supercapacitors.

Acknowledgements

This work is supported by U.S. Department of Energy. The authors thank Xiao Su for technical assistance with the XPS measurements, and Yuran Wang for the XRD measurements.

References

[1] P. Simon, Y. Gogotsi, *Nat Mater* **2008**, *7*, 845.
[2] G. P. Wang, L. Zhang, J. J. Zhang, *Chem Soc Rev* **2012**, *41*, 797.
[3] J. R. Miller, P. Simon, *Science* **2008**, *321*, 651.

[4] Y. P. Zhai, Y. Q. Dou, D. Y. Zhao, P. F. Fulvio, R. T. Mayes, S. Dai, *Adv Mater* **2011**, *23*, 4828.
[5] X. Zhao, B. M. Sanchez, P. J. Dobson, P. S. Grant, *Nanoscale* **2011**, *3*, 839.
[6] R. Liu, J. Duay, S. B. Lee, *Chem Commun* **2011**, *47*, 1384.
[7] A. L. M. Reddy, S. R. Gowda, M. M. Shaijumon, P. M. Ajayan, *Adv Mater* **2012**, *24*, 5045.
[8] Z. Q. Niu, P. S. Luan, Q. Shao, H. B. Dong, J. Z. Li, J. Chen, D. Zhao, L. Cai, W. Y. Zhou, X. D. Chen, S. S. Xie, *Energ Environ Sci* **2012**, *5*, 8726.
[9] M. Ertas, R. M. Walczak, R. K. Das, A. G. Rinzler, J. R. Reynolds, *Chem Mater* **2012**, *24*, 433.
[10] H. Zhang, G. Cao, Z. Wang, Y. Yang, Z. Shi, Z. Gu, *Electrochem Commun* **2008**, *10*, 1056.
[11] M. A. Q. Xue, F. W. Li, J. Zhu, H. Song, M. N. Zhang, T. B. Cao, *Adv Funct Mater* **2012**, *22*, 1284.
[12] L. Z. Fan, Y. S. Hu, J. Maier, P. Adelhelm, B. Smarsly, M. Antonietti, *Adv Funct Mater* **2007**, *17*, 3083.
[13] D.-W. Wang, F. Li, J. Zhao, W. Ren, Z.-G. Chen, J. Tan, Z.-S. Wu, I. Gentle, G. Q. Lu, H.-M. Cheng, *Acs Nano* **2009**, *3*, 1745.
[14] Y. G. Wang, H. Q. Li, Y. Y. Xia, *Adv Mater* **2006**, *18*, 2619.
[15] R. Liu, S. B. Lee, *J Am Chem Soc* **2008**, *130*, 2942.
[16] Z. Tang, C. H. Tang, H. Gong, *Adv Funct Mater* **2012**, *22*, 1272.
[17] H. Zhang, G. P. Cao, Z. Y. Wang, Y. S. Yang, Z. J. Shi, Z. N. Gu, *Nano Lett* **2008**, *8*, 2664.
[18] L. B. Hu, W. Chen, X. Xie, N. A. Liu, Y. Yang, H. Wu, Y. Yao, M. Pasta, H. N. Alshareef, Y. Cui, *Acs Nano* **2011**, *5*, 8904.
[19] X. Wang, A. Sumboja, M. F. Lin, J. Yan, P. S. Lee, *Nanoscale* **2012**, *4*, 7266.
[20] X. Y. Lang, A. Hirata, T. Fujita, M. W. Chen, *Nat Nanotechnol* **2011**, *6*, 232.
[21] C. Z. Yuan, L. Yang, L. R. Hou, L. F. Shen, X. G. Zhang, X. W. Lou, *Energ Environ Sci* **2012**, *5*, 7883.
[22] Q. Li, Z. L. Wang, G. R. Li, R. Guo, L. X. Ding, Y. X. Tong, *Nano Lett* **2012**, *12*, 3803.
[23] J. Y. Kim, K. Lee, N. E. Coates, D. Moses, T. Q. Nguyen, M. Dante, A. J. Heeger, *Science* **2007**, *317*, 222.
[24] U. Bach, D. Lupo, P. Comte, J. E. Moser, F. Weissortel, J. Salbeck, H. Spreitzer, M. Gratzel, *Nature* **1998**, *395*, 583.
[25] J. H. Ahn, H. S. Kim, K. J. Lee, S. Jeon, S. J. Kang, Y. G. Sun, R. G. Nuzzo, J. A. Rogers, *Science* **2006**, *314*, 1754.
[26] D. V. Talapin, C. B. Murray, *Science* **2005**, *310*, 86.
[27] X. F. Duan, C. M. Niu, V. Sahi, J. Chen, J. W. Parce, S. Empedocles, J. L. Goldman, *Nature* **2003**, *425*, 274.
[28] P. Poizot, S. Laruelle, S. Grugeon, L. Dupont, J. M. Tarascon, *Nature* **2000**, *407*, 496.
[29] L. B. Hu, J. W. Choi, Y. Yang, S. Jeong, F. La Mantia, L. F. Cui, Y. Cui, *Proc Natl Acad Sci U S A* **2009**, *106*, 21490.
[30] K. H. An, W. S. Kim, Y. S. Park, Y. C. Choi, S. M. Lee, D. C. Chung, D. J. Bae, S. C. Lim, Y. H. Lee, *Adv Mater* **2001**, *13*, 497.
[31] X. F. Lu, W. J. Zhang, C. Wang, T. C. Wen, Y. Wei, *Prog Polym Sci* **2011**, *36*, 671.
[32] C. D. Lokhande, D. P. Dubal, O. S. Joo, *Curr Appl Phys* **2011**, *11*, 255.
[33] Mao, X.; Rutledge, G. C.; Hatton, T. A., Submitted to Langmuir, Manuscript ID: la-2013-01440w

[34] T. Chen, L. Wang, G. H. Jiang, J. J. Wang, X. C. Dong, X. J. Wang, J. F. Zhou, C. L. Wang, W. Wang, *J Phys Chem B* **2005**, *109*, 4624.
[35] N. Lachman, X. M. Sui, T. Bendikov, H. Cohen, H. D. Wagner, *Carbon* **2012**, *50*, 1734.
[36] X. T. Zhang, J. R. Liu, B. Xu, Y. F. Su, Y. J. Luo, *Carbon* **2011**, *49*, 1884.
[37] X. Zhang, J. Zhang, Z. Liu, *Appl Phys a-Mater* **2005**, *80*, 1813.
[38] N. P. Blanchard, R. A. Hatton, S. R. P. Silva, *Chem Phys Lett* **2007**, *434*, 92.
[39] S. Suzuki, Y. Watanabe, T. Kiyokura, K. G. Nath, T. Ogino, S. Heun, W. Zhu, C. Bower, O. Zhou, *Phys Rev B* **2001**, *63*.
[40] J. J. Zhao, H. K. Park, J. Han, J. P. Lu, *J Phys Chem B* **2004**, *108*, 4227.
[41] C. C. Wang, G. Zhou, J. Wu, B. L. Gu, W. H. Duan, *Appl Phys Lett* **2006**, *89*.
[42] T. Wakahara, M. Sathish, K. Miyazawa, C. P. Hu, Y. Tateyama, Y. Nemoto, T. Sasaki, O. Ito, *J Am Chem Soc* **2009**, *131*, 9940.
[43] T. C. Leung, C. L. Kao, W. S. Su, Y. J. Feng, C. T. Chan, *Phys Rev B* **2003**, *68*.
[44] G. Lota, K. Fic, E. Frackowiak, *Energ Environ Sci* **2011**, *4*, 1592.
[45] M. D. Stoller, R. S. Ruoff, *Energ Environ Sci* **2010**, *3*, 1294.
[46] R. B. Rakhi, W. Chen, D. Y. Cha, H. N. Alshareef, *Nano Lett* **2012**, *12*, 2559.
[47] A. G. Pandolfo, A. F. Hollenkamp, *J Power Sources* **2006**, *157*, 11.

Figures:

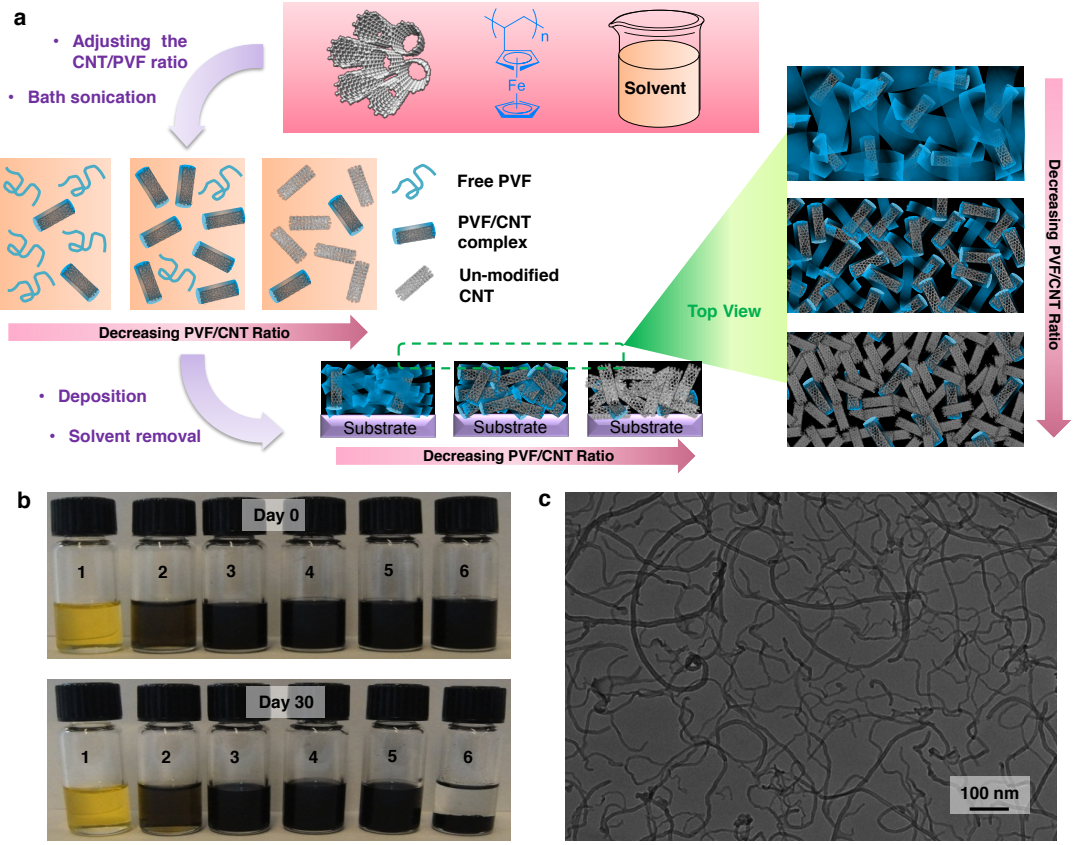

Figure 1. Fabrication of the PVF/CNT hybrids. (a) Schematic illustration of the solution process to fabricate PVF/CNT hybrids with different morphologies by varying the composition of the precusor inks. (b) Optical photos of PVF/CNT inks in chloroform on day 0 and day 30: from vial #1 to #6, CNT at 0, 0.03, 0.20, 0.67, 0.88, 0.20 mg/mL and PVF at 1, 0.97, 0.80, 0.33, 0.12, 0 mg/mL. (c) A transmission electron microscopy (TEM) image of a PVF/CNT dispersion (0.80 mg mL^{-1} PVF and 0.20 mg mL^{-1} CNT).

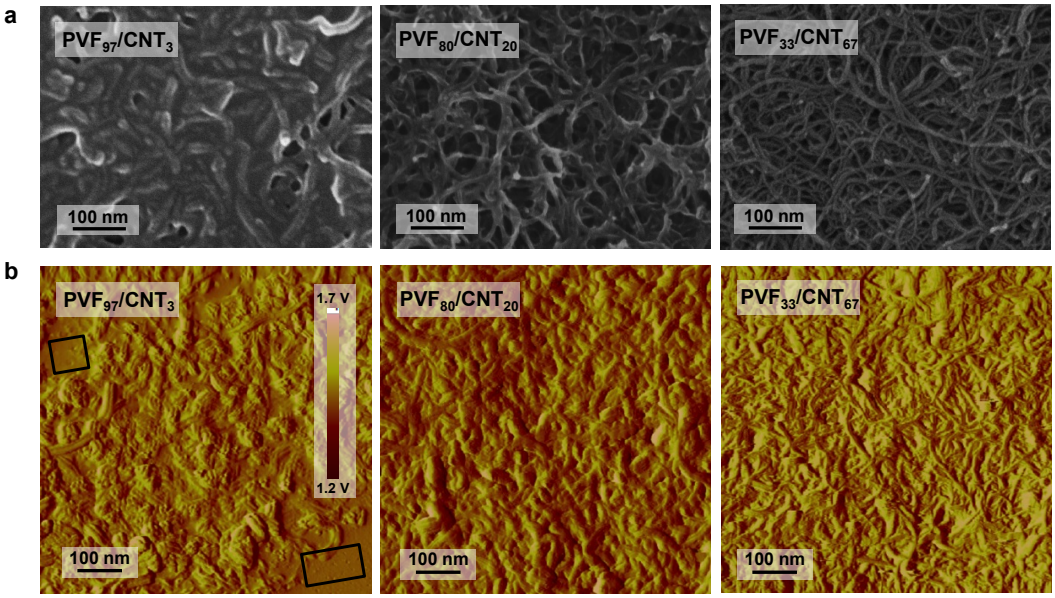

Figure 2. Morphological characteriztion of the PVF/CNT hybrids with varying compositions. (a) High-resolution scanning electron microscopy (HR-SEM) images and (b) atomic force microscopy (AFM) amplitude images of PVF_{97}/CNT_3, PVF_{80}/CNT_{20}, and PVF_{33}/CNT_{67}.

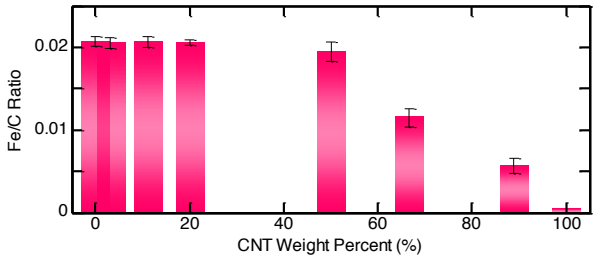

Figure 3. The Fe/C ratios of the PVF/CNT hybrids with varying compositions, calculated from their X-ray photoelectron spectra (XPS). Error bar: s.d. from three or four samples.

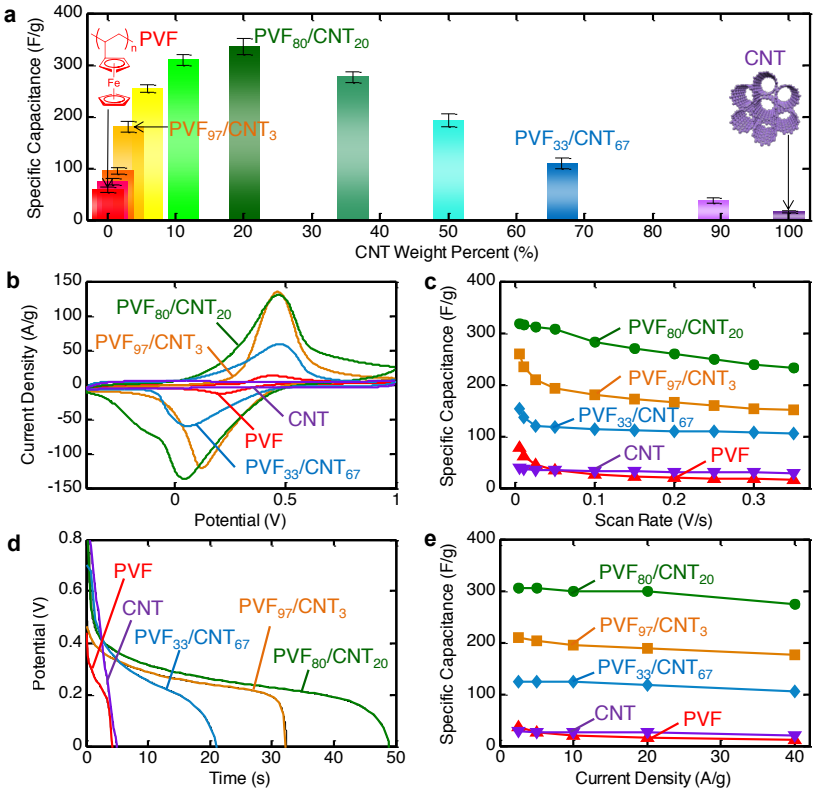

Figure 4. Composition-dependent electrocapacitive properties of the PVF/CNT hybrids. (a) The specific capacitance as a function of CNT composition, in weight percent. The capacitances were calculated from cyclic voltammograms at a scan rate of 20 mV/s. Error bar: s.d. from three samples. (b) Cyclic voltammograms (at a scan rate of 200 mV/s), (c) capacitance versus scan rate (the corresponding cyclic voltammograms are shown in **Figure S9)**, (d) galvanostatic discharge profiles (at a current density of 5 A/g), and (e) capacitance versus current density (the corresponding discharge profiles are shown in **Figure S10)** for PVF_{33}/CNT_{67}, PVF_{80}/CNT_{20}, PVF_{97}/CNT_3, PVF and CNT.

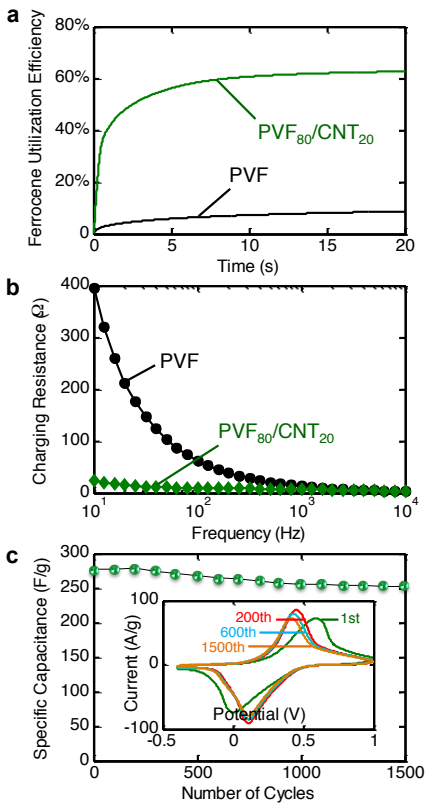

Figure 5. Electrochemical characterization of PVF_{80}/CNT_{20}. (a) Ferrocene utilization efficiency as a function of oxidation time. (b) Charging resistance versus frequency. (c) Capacitance versus the number of charge/discharge cycles. Inset shows cyclic voltammograms after the 1st, 200th, 600th, and 1500th cycle during the charging-discharging measurements.

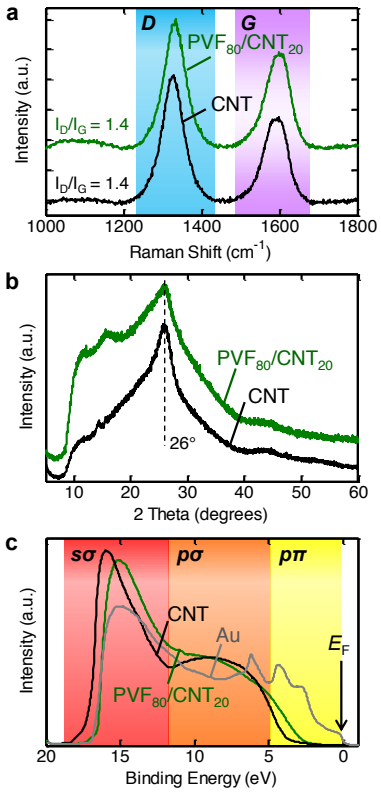

Figure 6. Microstructural characterization of PVF_{80}/CNT_{20}. (a) Raman spectra, (b) X-ray diffraction (XRD) patterns, and (c) ultraviolet photoelectron spectra (UPS) of PVF_{80}/CNT_{20} as well as pristine CNTs as a control. The UPS spectra were normalized to the integral area under the curves from 0 to 20 eV and gold was used as the internal standard to locate the Fermi level (0 eV).

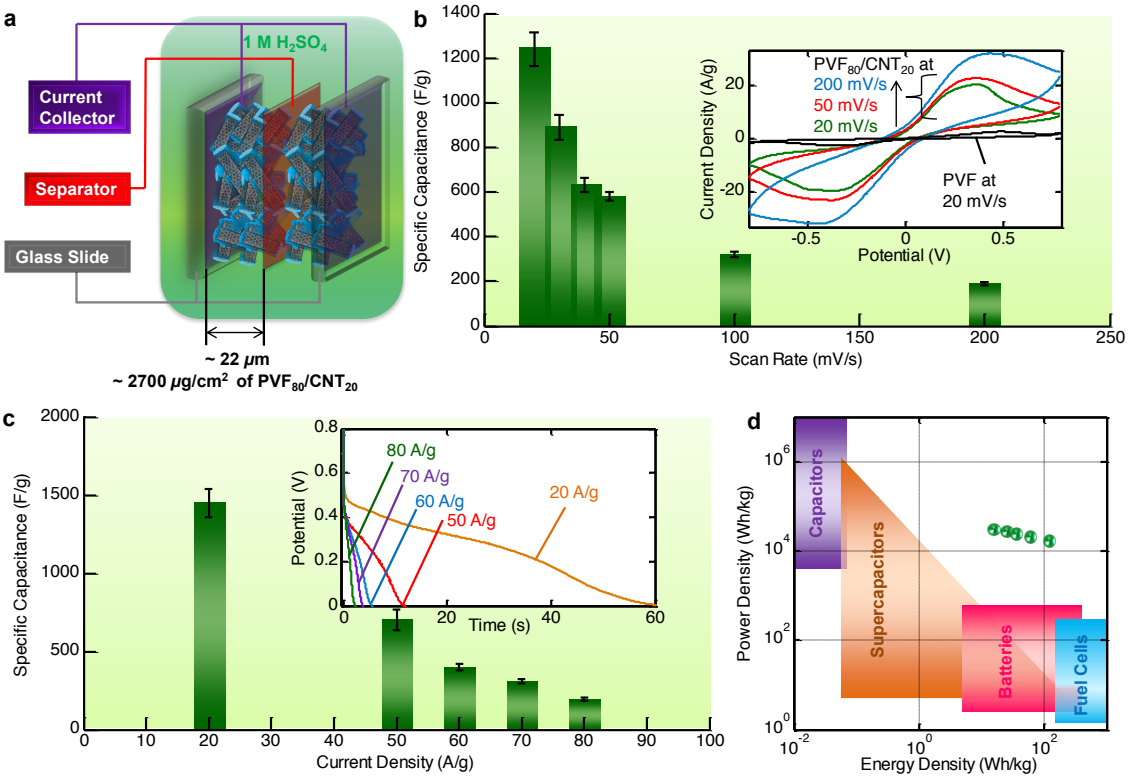

Figure 7. Supercapacitor cell performance of PVF_{80}/CNT_{20}. (a) Schematic illustration of a two-electrode configuration. (b) Specific capacitance versus scan rate, derived from cyclic voltammetry. Error bar: s.d. of three samples. Inset shows the cyclic voltammograms of PVF_{80}/CNT_{20} and PVF**.** (c) Specific capacitance versus current density, derived from galvanostatic measurements. Error bar: s.d. of three samples. Inset shows the discharge profiles at different current densities. (d) Ragone plot (power density versus energy density), derived from galvanostatic measurements. {is this your data shown in green? Best to say so explicitly}The ranges reported for common classes of energy storage devices[47] are also shown.

Graphical and textual abstract for table of contents

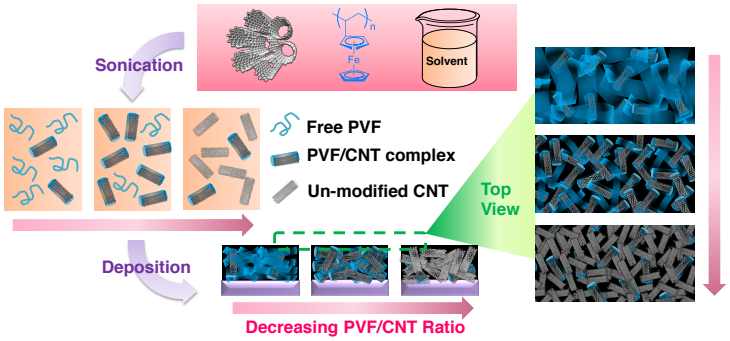

We report a metallocene/carbon hybrid system amenable to solution processing, whose nanostructure and electrochemical properties can be adjusted through manipulation of the ink composition. The hybrid with optimal perforamnce exhibits remarkable synergistic effects and unusually high capacitive energy storage capabilites.